ACS NANO
Cite This: ACS Nano 2018, 12, 4736–4743
www.acsnano.org

ARTICLE

Reducing Coercive-Field Scaling in Ferroelectric Thin Films *via* Orientation Control

Ruijuan Xu,[†] Ran Gao,[†] Sebastian E. Reyes-Lillo,[§,⊥,∥] Sahar Saremi,[†] Yongqi Dong,[▽] Hongling Lu,[†] Zuhuang Chen,[†] Xiaoyan Lu,[○] Yajun Qi,[◇] Shang-Lin Hsu,[†,‡] Anoop R. Damodaran,[†] Hua Zhou,[□] Jeffrey B. Neaton,[⊥,∥,¶] and Lane W. Martin*[,†,‡]

[†]Department of Materials Science and Engineering, University of California, Berkeley, California 94720, United States
[‡]Materials Sciences Division, Lawrence Berkeley National Laboratory, Berkeley, California 94720, United States
[§]Departamento de Ciencias Físicas, Universidad Andres Bello, Santiago 837-0136, Chile
[⊥]Department of Physics, University of California, Berkeley, California 94720, United States
[∥]Molecular Foundry, Lawrence Berkeley National Laboratory, Berkeley, California 94720, United States
[▽]National Synchrotron Radiation Laboratory and CAS Key Laboratory of Materials for Energy Conversion, University of Science and Technology of China, Hefei 230026, China
[○]School of Civil Engineering, Harbin Institute of Technology, Harbin 150001, China
[◇]Department of Materials Science and Engineering, Hubei University, Wuhan 430062, China
[□]X-ray Science Division, Advanced Photon Source, Argonne National Laboratory, Argonne, Illinois 60439, United States
[¶]Kavli Energy NanoScience Institute at Berkeley, Berkeley, California 94720, United States

Supporting Information

ABSTRACT: The desire for low-power/voltage operation of devices is driving renewed interest in understanding scaling effects in ferroelectric thin films. As the dimensions of ferroelectrics are reduced, the properties can vary dramatically, including the robust scaling relationship between coercive field (E_c) and thickness (d), also referred to as the Janovec–Kay–Dunn (JKD) law, wherein $E_c \propto d^{-2/3}$. Here, we report that whereas (001)-oriented heterostructures follow JKD scaling across the thicknesses range of 20–330 nm, (111)-oriented heterostructures of the canonical tetragonal ferroelectric $PbZr_{0.2}Ti_{0.8}O_3$ exhibit a deviation from JKD scaling wherein a smaller scaling exponent for the evolution of E_c is observed in films of thickness $\lesssim$ 165 nm. X-ray diffraction reveals that whereas (001)-oriented heterostructures remain tetragonal for all thicknesses, (111)-oriented heterostructures exhibit a transition from tetragonal-to-monoclinic symmetry in films of thickness $\lesssim$ 165 nm as a result of the compressive strain. First-principles calculations suggest that this symmetry change contributes to the deviation from the expected scaling, as the monoclinic phase has a lower energy barrier for switching. This structural evolution also gives rise to changes in the c/a lattice parameter ratio, wherein this ratio increases and decreases in (001)- and (111)-oriented heterostructures, respectively, as the films are made thinner. In (111)-oriented heterostructures, this reduced tetragonality drives a reduction of the remanent polarization and, therefore, a reduction of the domain-wall energy and overall energy barrier to switching, which further exacerbates the deviation from the expected scaling. Overall, this work demonstrates a route toward reducing coercive fields in ferroelectric thin films and provides a possible mechanism to understand the deviation from JKD scaling.

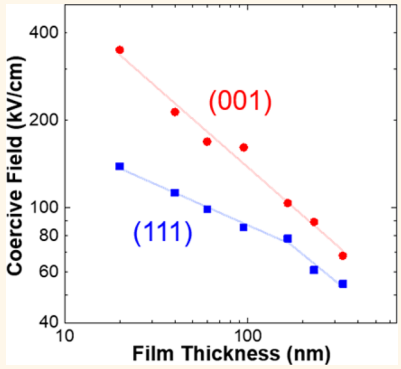

KEYWORDS: *ferroelectric, thin film, size effects, coercive-field scaling, X-ray diffraction*

Ferroelectric thin films, which possess an electrically switchable spontaneous polarization, have garnered increasing attention for applications in modern nanoelectronics. Such materials have been utilized as critical components in nonvolatile memories[1,2] and logic devices,[3,4] exhibiting improved performance[5−7] such as high-speed write operation, long-term endurance, and low-voltage operation. With the increasing requirement for storage density and power efficiency in these devices, it is essential to investigate the scaling potential of ferroelectric thin films for low-voltage

Received: February 21, 2018
Accepted: April 11, 2018
Published: April 11, 2018

DOI: 10.1021/acsnano.8b01399
ACS Nano 2018, 12, 4736–4743

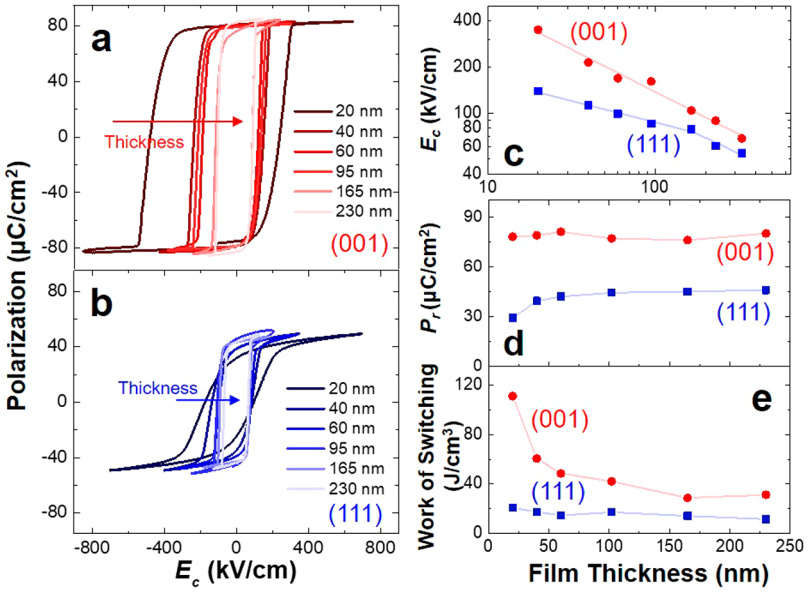

Figure 1. Ferroelectric hysteresis loops measured at 1 kHz for (a) (001)- and (b) (111)-oriented heterostructures as a function of film thickness. (c) Coercive field (E_c), (d) remanent polarization (P_r), and (e) work of switching plotted as a function of film thickness for (001)- and (111)-oriented heterostructures.

operation and low power consumption. In particular, it is possible to accomplish low-voltage operation in ferroelectrics simply by reducing film thickness. Such a variation of coercive field with thickness pertains to ferroelectric size effects, or the change in properties with decreasing physical dimension, which have been widely observed in ferroelectric ceramics,[8] single crystals,[19,20] and thin films.[9−13] While early work on thin and ultrathin versions of these materials was susceptible to extrinsic size effects, such as interfacial "dead layers", which lead to suppressed ferroelectricity,[14−16] recent advances in contact materials, as well as material synthesis,[17,18] have produced increasingly high-quality ferroelectric thin films that beget the study of intrinsic size effects.

One of the foremost intrinsic size-effect phenomena is the scaling relationship between coercive field (E_c) and film thickness (d), or the so-called Janovec−Kay−Dunn (JKD) law, wherein $E_c \propto d^{-2/3}$. This semiempirical relation derived in the 1960s from studies of ferroelectric single crystals was later found to be applicable to thin films from 100 μm to 100 nm thick.[19−21] Despite the vast majority of materials explored to date following this scaling law, occasional studies have found deviations.[22−24] For example, work on ultrathin films of poly(vinylidene fluoride trifluoroethylene) reported a deviation from JKD scaling wherein the measured E_c was independent of thickness in films of thickness < 15 nm.[22,23] Later work, however, found that such deviations could be accounted for by considering depolarization fields arising from incomplete screening from electrodes, which leads to a difference between the measured and true E_c in ultrathin films.[25] Despite the seeming universality of JKD scaling, its semiempirical nature leaves the door open to the identification of systems that deviate from this behavior and thus provide even better low-voltage operation. How to engineer materials to achieve such reduced E_c scaling remains a challenge.

Here, using a combination of advanced thin-film epitaxy, X-ray diffraction, and first-principles calculations, the effect of film orientation on E_c scaling in tetragonal $PbZr_{0.2}Ti_{0.8}O_3$ thin films is probed. In this work, we report that while (001)-oriented heterostructures follow JKD scaling across the thickness range of 20−330 nm, (111)-oriented heterostructures exhibit a deviation from JKD scaling wherein a reduced scaling exponent for the evolution of E_c is observed in films of thickness $\lesssim$ 165 nm. X-ray diffraction reveals that, whereas (001)-oriented heterostructures remain tetragonal for all thicknesses, (111)-oriented heterostructures exhibit a transition from tetragonal-to-monoclinic symmetry in films of thickness $\lesssim$ 165 nm as a result of the compressive strain. First-principles calculations suggest that this symmetry change contributes to the deviation from the expected scaling as the monoclinic phase has a lower energy barrier for switching. This structural evolution also gives rise to changes in the c/a lattice parameter ratio, wherein this ratio increases and decreases in (001)- and (111)-oriented heterostructures, respectively, as the films are made thinner. In (111)-oriented heterostructures, this reduced tetragonality drives a reduction of the remanent polarization and, therefore, a reduction of the domain-wall energy and overall energy barrier to switching, which further exacerbates the deviation from the expected scaling.

RESULTS AND DISCUSSION

The 80 nm $La_{0.7}Sr_{0.3}MnO_3$/20−330 nm $PbZr_{0.2}Ti_{0.8}O_3$/20 nm $La_{0.7}Sr_{0.3}MnO_3$/$SrTiO_3$ (001) and (111) heterostructures were grown *via* pulsed-laser deposition using established procedures (Methods).[26,27] All film thicknesses were measured using both X-ray reflectivity and Rutherford backscattering spectrometry (Supporting Information, Figures S1 and S2). Following growth, the top $La_{0.7}Sr_{0.3}MnO_3$ layer was further patterned into 25 μm (diameter) circular electrodes using a wet-etching process (Methods). Ferroelectric hysteresis loop measurements (Methods) were performed as a function of frequency on all heterostructures (for simplicity, only loops measured at 1 kHz are shown here for (001)- (Figure 1a) and (111)-oriented (Figure 1b) heterostructures). Hysteresis loops measured at other frequencies are also provided (Supporting Information, Figures S3 and S4). Regardless of the film thickness and orientation, well-saturated hysteresis loops can be measured

DOI: 10.1021/acsnano.8b01399
ACS Nano 2018, 12, 4736−4743

down to 1 Hz, indicating the films are highly insulating. The E_c, defined as $(|E_c^+| - |E_c^-|)/2$ (where $|E_c^+|$ and $|E_c^-|$ are the magnitudies of the positive and negative E_c values, respectively), is plotted as a function of thickness for all the (001)- and (111)-oriented heterostructures (Figure 1c). A number of key observations can be made. First, for all film thicknesses, the (111)-oriented heterostructures exhibit lower E_c than (001)-oriented heterostructures. This could be related to different local-switching events in these differently oriented films, as prior studies[27] have found that direct 180° switching is favored in (001)-oriented heterostructures, whereas multistep, 90° switching is favored in (111)-oriented heterostructures. These 90° switching events, which have a lower energy barrier, could contribute to a lower E_c in the (111)-oriented heterostructures. Second, clear differences are observed in the E_c scaling for the two film orientations. In (001)-oriented heterostructures, $E_c \propto d^{-0.55\pm0.032}$ across the entire thickness regime studied herein, which is close to the expected JKD scaling. In the (111)-oriented heterostructures, $E_c \propto d^{-0.51\pm0.013}$ for films of thickness > 165 nm and $E_c \propto d^{-0.28\pm0.019}$ for films of thickness < 165 nm. In addition, the remanent polarization P_r, defined as $(P_r^+ - P_r^-)/2$ (where P_r^+ and P_r^- are the positive and negative P_r values, respectively), remains essentially unchanged in (001)-oriented heterostructures, but decreases in (111)-oriented heterostructures as the film thickness is reduced (Figure 1d). The work of switching, as defined as the area inside the hysteresis loop and a direct measure of the energy loss during switching (Figure 1e), increases rapidly as the films are made thinner for the (001)-oriented heterostructures, but remains essentially unchanged for the (111)-oriented heterostructures. The difference in the work of switching is particularly large in the thinnest films, where, in (111)-oriented heterostructures, the greatly reduced E_c and P_r dominate the response. Ultimately, what these data suggest is that the E_c scaling for (111)-oriented heterostructures deviates from the expected JKD scaling, and this, in turn, manifests itself as a dramatic reduction of the work of switching in the thinnest films. This observation is particularly important from an engineering standpoint, but begs the question as to what causes this deviation in the scaling relation in (111)-oriented heterostructures.

Before this deviation can be attributed to an intrinsic feature of the material, we must explore the possibility that this deviation is caused by extrinsic factors. Possible extrinsic factors such as interfacial "dead layers" and incomplete screening from electrodes, however, are excluded for the following reasons: In the case of an interfacial "dead layer", an extra voltage drop can be observed, which leads to an increase in E_c and a larger exponent in E_c scaling ($E_c \propto d^{-1}$).[16,24] Additionally, the $La_{0.7}Sr_{0.3}MnO_3$ electrodes were controlled to be of sufficient thickness to provide sufficient carriers to screen the polarization, were produced *in situ* during the same growth process as the ferroelectric layer, and were created using identical conditions to purposely make them as identical as possible. Thus, it is unlikely that the observed deviation is caused by incomplete screening from electrodes that occurs only in the (111)-oriented heterostructures. Having ruled out such extrinsic factors, we focus on investigating possible intrinsic factors that could lead to the observed deviation. First, we performed X-ray rocking curve measurements to study whether the observed deviation could be related to variations in the film crystalline quality (Supporting Information, Figure S5). It is noted that the full-width at half-maximum (FWHM) of the rocking curves, which is indicative of the crystalline quality, evolves in a similar manner with film thickness for both film orientations, such that 20-nm-thick films of both orientations show small and similar FWHM (<0.05°). Recall, however, that the largest deviation from the expected JKD scaling occurs in 20-nm-thick (111)-oriented heterostructures, not the (001)-oriented heterostructure; suggesting that the crystalline quality is not the cause for the observed deviation from JKD scaling.

In an attempt to better understand the driving force for this deviation from JKD scaling, X-ray diffraction experiments were completed to explore a further potential structural origin. First, for (001)-oriented heterostructures, analysis of the 001-diffraction conditions for the $PbZr_{0.2}Ti_{0.8}O_3$ films reveals that as the film thickness is reduced, the out-of-plane lattice parameter elongates (as expected for a compressively strained film that is coherently strained only in the thinnest films; Supporting Information, Figure S6). Reciprocal space mapping (RSM) studies were used to examine the evolution of both the in-plane and out-of-plane lattice parameters for the (001)-oriented heterostructures, and, for brevity, only RSMs of the 103-diffraction conditions of the films and substrate for films of thickness of 40 nm (Figure 2a) and 165 nm (Figure 2b) are

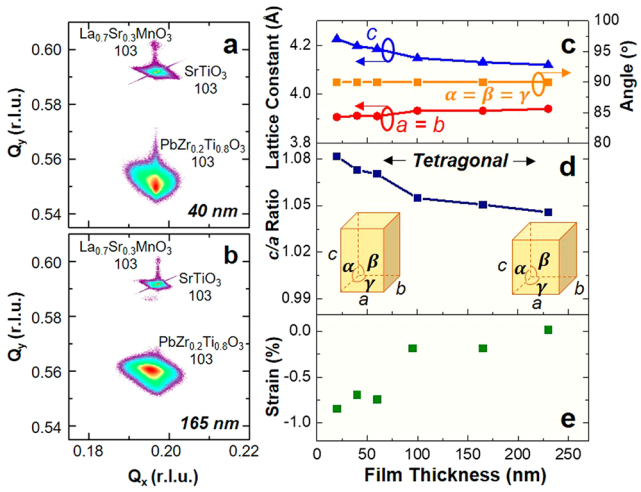

Figure 2. X-ray reciprocal space mapping studies of the 103-diffraction conditions of films and substrates for (001)-oriented $PbZr_{0.2}Ti_{0.8}O_3$ heterostructures of thickness (a) 40 nm and (b) 165 nm. Thickness dependence of (c) lattice constants and interaxial angles, (d) c/a ratio, and (e) self-strain in (001)-oriented heterostructures.

shown (RSMs for all thicknesses are provided elsewhere; Supporting Information, Figure S7). For the $PbZr_{0.2}Ti_{0.8}O_3$ films of thickness $\lesssim$60 nm, the 103-diffraction peaks arising from the $PbZr_{0.2}Ti_{0.8}O_3$ and $SrTiO_3$ exhibit the same in-plane values, confirming the films are coherently strained. For the $PbZr_{0.2}Ti_{0.8}O_3$ films of thickness $\gtrsim$ 60 nm, the 103-diffraction peak for the $PbZr_{0.2}Ti_{0.8}O_3$ is found to shift toward smaller Q_x values, indicating that the films are relaxing. A summary of the evolution of the lattice with film thickness, namely, the evolution of the in-plane (a, b) and out-of-plane (c) lattice parameters as well as the lattice angle (α, β, and γ, the interaxial angles) (Figure 2c) and the c/a lattice parameter ratio (Figure 2d), is provided. It is found that, as the film thickness decreases, c increases and a (or b, $a = b$) decreases, resulting in an increasing c/a ratio, while α, β, $\gamma \approx 90°$, implying that the

DOI: 10.1021/acsnano.8b01399
ACS Nano 2018, 12, 4736–4743

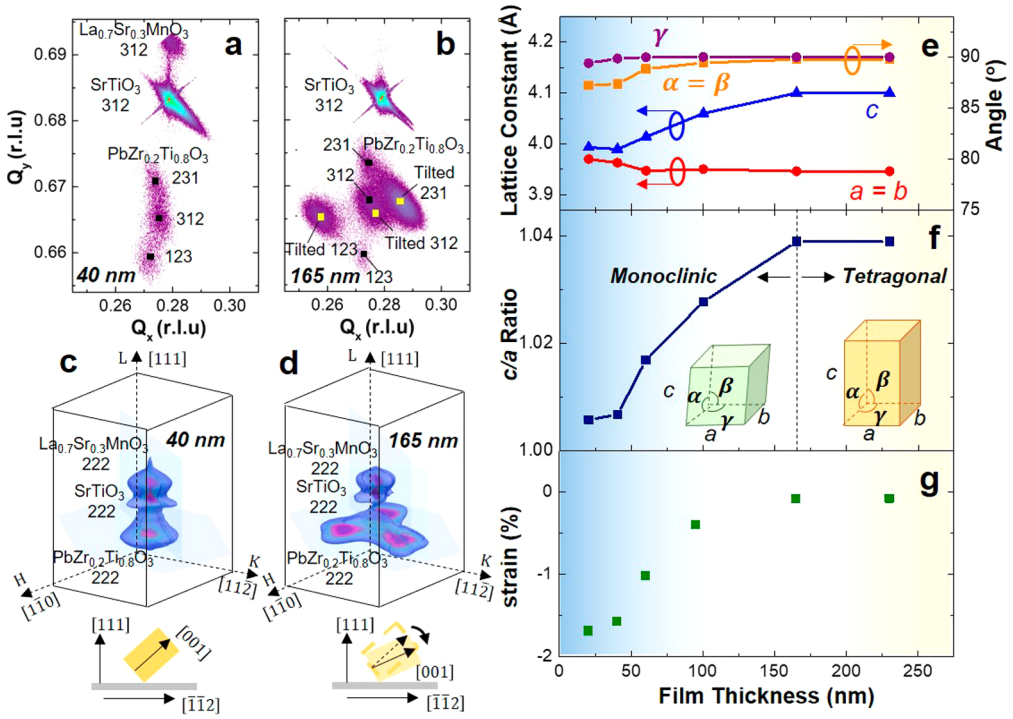

Figure 3. X-ray reciprocal space mapping studies about the 312-diffraction conditions of films and substrates for (111)-oriented $PbZr_{0.2}Ti_{0.8}O_3$ heterostructures of thickness (a) 40 nm and (b) 165 nm. Three-dimensional reciprocal space mapping studies about the 222-diffraction conditions of films and substrates for (111)-oriented $PbZr_{0.2}Ti_{0.8}O_3$ heterostructures of thickness (c) 40 nm and (d) 165 nm. Thickness dependence of (e) lattice constants and interaxial angles, (f) *c*/*a* ratio, and (g) self-strain in (111)-oriented heterostructures.

structure remains tetragonal. Using the measured and bulk lattice parameter values, we can calculate the effective self-strain (*i.e.*, the distortion of the lattice relative to bulk) as a function of thickness ($\varepsilon = \frac{a_{measured} - a_{bulk}}{a_{bulk}}$). It is noted that the effective compressive strain in the film increases with reducing film thickness (Figure 2e).

Similar studies were performed for the (111)-oriented heterostructures. Analysis of the 111-diffraction conditions shows no obvious trend and thus provides limited insights into any structural changes (Supporting Information, Figure S8). RSM studies on the 312- and 330-diffraction conditions of the $PbZr_{0.2}Ti_{0.8}O_3$ films were completed to probe the lattice evolution along the (orthogonal) in-plane $[1\bar{1}0]$ and $[11\bar{2}]$, respectively. Again, for brevity, only RSMs of the 312-diffraction condition of the films of thickness of 40 nm (Figure 3a) and 165 nm (Figure 3b) are shown (RSMs of the 312- and 330-diffraction conditions for all thicknesses are provided elsewhere; Supporting Information, Figures S9 and S10, respectively). Complex diffraction patterns were observed for the 312-diffraction condition wherein the $PbZr_{0.2}Ti_{0.8}O_3$ peak splits into three peaks in films of thickness $\lesssim$ 60 nm and six peaks in films of thickness $\gtrsim$ 60 nm. It should be noted that for (111)-oriented versions of tetragonal $PbZr_{0.2}Ti_{0.8}O_3$ three structural variants are present with the polar axis (*c* lattice parameter) aligned along the [100], [010], and [001], which could contribute to the splitting of the 312-diffraction peaks into three peaks, which are indexed as the 312-, 231-, and 123-diffraction conditions (Figure 3a and b). This mechanism, however, can only account for the splitting into three peaks in films of thickness $\lesssim$ 60 nm. In order to understand the additional peak splitting in thicker films, three-dimensional RSM studies were completed for the 222-diffraction condition (Methods). For brevity, only three-dimensional RSMs for films of thickness of 40 nm (Figure 3c) and 165 nm (Figure 3d) are shown (three-dimensional RSMs for all thicknesses for the 222-diffraction conditions are provided elsewhere; Supporting Information, Figure S11). In such RSMs, clear 3-fold splitting of the $PbZr_{0.2}Ti_{0.8}O_3$ 222-diffraction peaks was observed in the *HK* mapping for films of thickness $\gtrsim$ 60 nm (Supporting Information, Figure S12). The three structural variants in the $PbZr_{0.2}Ti_{0.8}O_3$ films are indistinguishable under the on-axis 222-diffraction condition due to the fact that they have the same lattice projections along [222], such that the on-axis peak splitting can only be explained by a unit-cell tilt wherein the unit cells are inclined toward the $\langle 11\bar{2} \rangle$ with 3-fold symmetry within the plane (schematics, Figure 3c and d). The tilting angles can be further analyzed from the *KL* mapping, which shows increasing tilting with increasing film thickness (Supporting Information, Figures S13 and S14). In turn, a comprehensive picture of the structure of the films with thickness $\gtrsim$ 60 nm is produced wherein they include three structural variants and three tilted versions of those variants. Similar analysis is also applicable to RSM results measured for the $PbZr_{0.2}Ti_{0.8}O_3$ 330-diffraction condition (Supporting Information, Figure S10). These fully indexed diffraction results allow for the extraction of a similar summary of the evolution of the lattice with film thickness, namely, the evolution of *a*, *b*, and *c* as well as the interaxial angles α, β, and γ (Figure 3e) and the *c*/*a* lattice parameter ratio (Figure 3f). Here, *c* decreases while *a* (or *b*, *a* = *b*) increases, resulting in a decreasing *c*/*a* ratio with reducing film thickness (the opposite trend of that observed for the (001)-oriented heterostructures). The lattice angles also evolve differently, wherein the α (or β, $\alpha = \beta$) and γ angles deviate from 90° upon reducing the film thickness, which leads to a tetragonal-to-

DOI: 10.1021/acsnano.8b01399
ACS Nano 2018, 12, 4736−4743

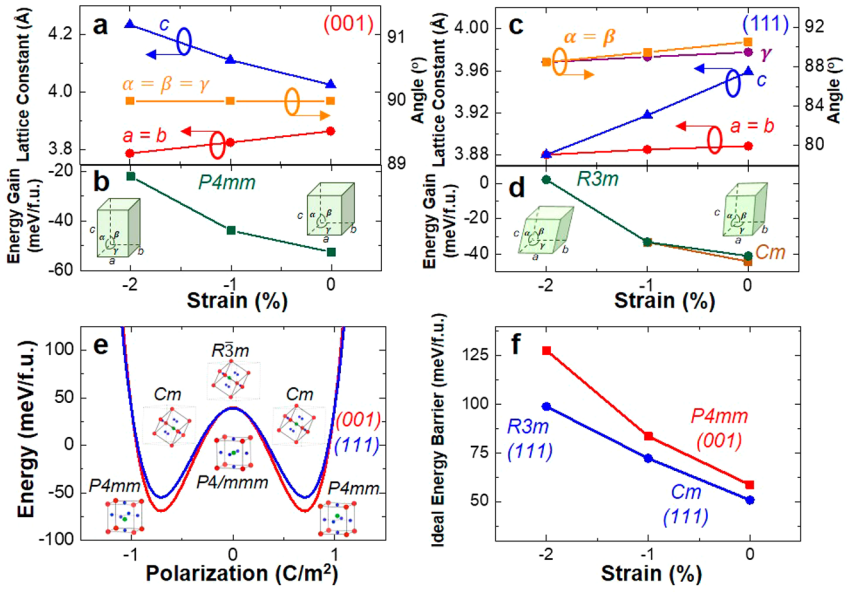

Figure 4. DFT calculations of lattice constants and stable structures, respectively, in (a, b) (001)- and (c, d) (111)-oriented heterostructures as a function of strain. (e) Ideal energy barrier for (001)- and (111)-oriented heterostructures. (f) Calculated energy barrier as a function of strain in the (001)- and (111)-oriented heterostructures.

monoclinic structural transition below ∼165 nm. The α and γ angles decrease further with reducing film thickness, implying the monoclinic structure trends toward a rhombohedral structure. Using the measured and bulk lattice parameters, the effective self-strain (*i.e.*, the distortion of the lattice relative to bulk) can be extracted as a function of film thickness. Since the in-plane strain applied in the (111)-oriented heterostructures is not isotropic, we analyzed the average in-plane self-strain using the average lattice parameter along ⟨110⟩ (Supporting Information, Figure S15 and Table S1). Similar to the (001)-oriented heterostructures, it is noted that the compressive self-strain increases with reducing film thickness (Figure 3g). All told, these structural analyses reveal that the structure of the (001)- and (111)-oriented heterostructures evolves differently in two major ways: (1) Upon reducing the film thickness, the (001)-oriented heterostructures remain tetragonal, whereas the (111)-oriented heterostructures undergo a tetragonal-to-monoclinic structural evolution. (2) The c/a ratio evolves in an opposite trend wherein an increasing and a decreasing c/a ratio are observed as the thickness is reduced in (001)- and (111)-oriented heterostructures, respectively.

Next, we studied whether and how these two structural observations are related to the observed deviation from JKD scaling. First-principles density functional theory (DFT) calculations were performed to reveal the correlation between the structural changes and the evolution of the switching properties. Our DFT calculations captured the effects of strain on $PbTiO_3$ *via* a compressive strain within the (001) and (111) (referred to as (001)-strain and (111)-strain, respectively) to simulate (001)- and (111)-oriented heterostructures, respectively. For (001)-strain, c is computed to increase while a (or b, $a = b$) decreases, resulting in an increasing c/a ratio with increasing compressive strain (Figure 4a). At the same time, $\alpha = \beta = \gamma = 90°$ irrespective of the magnitude of the strain; thus, the ground-state structure remains the tetragonal *P4mm* phase (Figure 4b) for all compressive strains considered, consistent with the experimental observations (Figure 2a). For (111)-strain, even at zero strain, due to the substrate clamping effect, the symmetry is lowered to a monoclinic *Cm* structure wherein α (or β, $\alpha = \beta$) and γ deviate slightly from 90° (*i.e.*, a monoclinically distorted *P4mm* structure is produced at zero strain) (Figure 4c and d). Upon increasing the magnitude of the compressive strain (simulating reduced film thickness), both c and a (or b, $a = b$) are computed to decrease (with c decreasing at a faster rate, thus resulting in a decreasing c/a ratio) and finally converge to the same value at ∼−2% strain, wherein the monoclinic *Cm* structure transforms to a rhombohedral *R3m* structure. At the same time, α and γ also decrease in magnitude and converge to the same value with increasing compressive strain (or reduced film thickness). The overall structural evolution predicted by the DFT calculations is consistent with our experiments on (111)-oriented heterostructures, wherein the ground state adopts a monoclinic structure and trends toward a rhombohedral structure when subjected to a (111)-strain (Figure 3). Furthermore, from the DFT calculations, it is possible to estimate the energy barrier for switching (as extracted from the double-well energy curve, defined as the energy difference between the local ferroelectric minima and the paraelectric saddle-point configurations, *i.e.*, *P4/mmm* and *R3̄m*, respectively) for the *P4mm* and *Cm* structures (Figure 4e). Plotting the ideal energy barrier as a function of strain, it is noted that the *Cm* structure not only exhibits lower energy barriers at all strains but also increases with increasing compressive strain at a lower rate than does the energy barrier for the *P4mm* structure (Figure 4f). In turn, a lower energy barrier for switching would translate to a lower E_c, and, thus, this could potentially play a role in the observed deviation from JKD scaling in the (111)-oriented heterostructures.

We note, however, that this simple explanation ignores a number of effects known to impact switching in ferroelectrics (*e.g.*, differences in interfacial "dead layer" effects, incomplete screening from electrodes, defect densities, crystalline quality, *etc.*), many of which we have already addressed and have shown to be unlikely explanations for the observations. Ultimately, for the (111)-oriented heterostructures of thickness $\gtrsim$ 165 nm, the

DOI: 10.1021/acsnano.8b01399
ACS Nano 2018, 12, 4736−4743

film adopts a relaxed tetragonal structure and exhibits a similar scaling behavior to the (001)-oriented heterostructures that follow JKD scaling. Upon reducing the film thickness, due to the effects of epitaxial strain, the film transforms to a monoclinic structure and gradually trends toward a rhombohedral structure (wherein the lattice tilt angles deviate more from 90°) with strain. Such a structural transition leads to the change in the fundamental energy barrier for switching that could potentially contribute to the observed scaling behavior. In addition to the observed structural transition contributing to the scaling deviation, the thickness-dependent evolution of the c/a ratio also likely impacts the scaling relation. Recall that in the (001)-oriented heterostructures the c/a ratio increases with decreasing film thickness, but does not significantly affect P_r due to the large ionic displacement in (001)-oriented $PbZr_{0.2}Ti_{0.8}O_3$ films, which is insensitive to such structural changes.[11] On the other hand, in the (111)-oriented heterostructures, the c/a ratio decreases with decreasing film thickness, and this reduction in tetragonality drives a reduction in P_r. This reduction of P_r could also be exacerbated by the presence of a flexoelectric effect, which arises from the partial relaxation of strain in the thin (111)-oriented heterostructures.[28] It has been shown that the thermodynamic E_c scales directly with P_r because changes in P_r can drive corresponding changes in the domain-wall energy. Thus, lowering the P_r would decrease the domain-wall energy and, in turn, the energy barrier for switching.[13,29] With this in mind, we include the effects of P_r variation in an adapted version of JKD scaling by multiplying $d^{-2/3}$ by a prefactor P_{mea}/P_{max}, wherein P_{mea} refers to the measured P_r and P_{max} refers to the measured maximum polarization (*i.e.*, P_r measured for a 230 nm thick film). Note that P_{mea}/P_{max} also scales with thickness since both the c/a ratio evolution and the strain gradient depend on the film thickness. The modified scaling relation matches closely the observed E_c evolution in (111)-oriented heterostructures (Supporting Information, Figure S16). Thus, our work suggests that the decreasing P_r can potentially contribute to the reduced E_c in (111)-oriented heterostructures. Although this approach can be simply accomplished in ultrathin films wherein a large depolarization field can destabilize and reduce P_r, such ultrathin films are usually difficult to measure due to the large leakage currents and extrinsic interface effects. That said, our work suggests a method to achieve the desired reduced E_c for ferroelectrics outside of this ultrathin limit by engineering the film orientation to induce both a structural transition and P_r reduction that can be combined to affect E_c dramatically.

CONCLUSION

In summary, our work studied the effects of film orientation on coercive-field scaling in tetragonal $PbZr_{0.2}Ti_{0.8}O_3$ thin films. We observed that while (001)-oriented heterostructures follow JKD scaling across the thickness range of 20−330 nm, (111)-oriented heterostructures of the canonical tetragonal ferroelectric $PbZr_{0.2}Ti_{0.8}O_3$ exhibit a deviation from JKD scaling wherein a smaller scaling exponent for the evolution of E_c is observed in films of thickness $\lesssim$ 165 nm. X-ray diffraction reveals that, while (001)-oriented heterostructures remain tetragonal for all thicknesses, (111)-oriented heterostructures exhibit a transition from tetragonal-to-monoclinic symmetry in films of thickness $\lesssim$ 165 nm as a result of the compressive strain. First-principles calculations suggest that this symmetry change contributes to the deviation from the expected scaling, as the monoclinic phase has a lower energy barrier for switching. This structural evolution also gives rise to changes in the c/a lattice parameter ratio, wherein this ratio increases and decreases in (001)- and (111)-oriented heterostructures, respectively, as the films are made thinner. In (111)-oriented heterostructures, this reduced tetragonality drives a reduction of the remanent polarization and, therefore, a reduction of the domain-wall energy and overall energy barrier to switching, which further exacerbates the deviation from the expected scaling. Overall, this work demonstrates a route toward reducing coercive fields in ferroelectric thin films and provides a possible mechanism to understand this deviation from JKD scaling.

METHODS

Heterostructure Growth. The 80 nm $La_{0.7}Sr_{0.3}MnO_3/x$ nm $PbZr_{0.2}Ti_{0.8}O_3$/20 nm $La_{0.7}Sr_{0.3}MnO_3$ heterostructures were grown on (001)- and (111)-oriented, single-crystalline $SrTiO_3$ substrates by pulsed-laser deposition using a KrF excimer laser (248 nm, LPX 300, Coherent), where the thickness of $PbZr_{0.2}Ti_{0.8}O_3$ varies in the range from 20 to 330 nm (*i.e.*, x = 20, 40, 60, 95, 165, 230, 330 nm). The growth of all film layers was carried out in a dynamic oxygen pressure of 200 mTorr, at a growth temperature of 650 °C, and a laser fluence and repetition rate of 1.0 J/cm^2 and 3 Hz, respectively. Following growth, the samples were cooled to room temperature at a cooling rate of 5 °C/min under a static oxygen pressure of 760 Torr.

Capacitor Fabrication. The circular top electrodes (diameter 25 μm) were fabricated using a wet etching method. First, the photoresist was patterned on the as-grown heterostructures using photolithography, which only covers the circular electrode regions. Using dilute H_3PO_4 acid (dilution ratio 1 part acid:5 parts water) the uncovered $La_{0.7}Sr_{0.3}MnO_3$ was etched away within 30 s, leaving circular $La_{0.7}Sr_{0.3}MnO_3$ contacts covered by the photoresist. Subsequently the photoresist was removed by acetone, leaving the circular $La_{0.7}Sr_{0.3}MnO_3$ electrodes.

Electrical Characterization. Ferroelectric polarization hysteresis loops were measured at room temperature using a Precision Multiferroic Tester (Radiant Technologies).

X-ray Analysis. A high-resolution X-ray diffractometer (Panalytical, X'Pert3MRD) was used to perform line scans and RSM studies. Synchrotron X-ray RSM studies were conducted at the Advanced Photon Source, Argonne National Laboratory, Sector 33-BM, and 12-ID-D using the Pilatus 100 K detector.

Computational Methods. First-principles DFT calculations were performed within the local density approximation[30] with pseudopotentials and a plane-wave basis, using the Vienna *Ab-Initio* Simulation Package (VASP).[31,32] Epitaxial strain within the (001) and (111) were simulated through strained bulk calculations in cubic and hexagonal unit cells with 5 and 15 atoms (*i.e.*, 1 and 3 formula units), respectively.[33−36] Misfit strain was measured with respect to the computed average in-plane lattice parameter: a_{bulk} = 3.865 Å for tetragonal $PbTiO_3$ under (001)-strain and a_{bulk} = 3.906 Å for monoclinic $PbTiO_3$ under (111)-strain. Structural relaxations were performed keeping the matching plane lattice vectors fixed: $\mathbf{a}_1 = (a, 0, 0)$ and $\mathbf{a}_2 = (0, a, 0)$ for (001)-strain and $\mathbf{a}_1 = (\sqrt{2}a, 0, 0)$ and $\mathbf{a}_2 = (-a/\sqrt{2}, \sqrt{3/2}\,a, 0)$ for (111)-strain, while the out-of-plane lattice vectors, $\mathbf{a}_3 = (0, 0, a)$ for (001)-strain and $\mathbf{a}_3 = (0, 0, \sqrt{3}a)$ for (111)-strain, along with the internal atomic positions were optimized until forces were smaller than 1 meV/Å.

Our VASP calculations use 6 × 6 × 6 and 5 × 5 × 5 Monkhorst−Pack k-point grids[37] for (001)- and (111)-strain, respectively, and a plane wave energy cutoff of 500 eV. The projected augmented wave pseudopotentials[38] explicitly include 14 valence electrons for Pb ($6s^25d^{10}6p^2$), 12 for Ti ($3s^23p^63d^24s^2$), and 6 for O ($2s^22p^4$). Berry-phase polarization calculations were performed within the modern theory of polarization, as implemented in VASP.[39]

DOI: 10.1021/acsnano.8b01399
ACS Nano 2018, 12, 4736−4743

ASSOCIATED CONTENT

Supporting Information

The Supporting Information is available free of charge on the ACS Publications website at DOI: 10.1021/acsnano.8b01399.

Film thickness calibration, ferroelectric hysteresis loop measurements, X-ray rocking curve measurements, X-ray structural analyses for (001)-oriented heterostructures, X-ray structural analyses for (111)-oriented heterostructures, calculation of average strain in (111)-oriented heterostructures, modified scaling relation, supporting computational results (PDF)

AUTHOR INFORMATION

Corresponding Author

*E-mail: lwmartin@berkeley.edu.

ORCID

Ruijuan Xu: 0000-0001-5046-0599

Zuhuang Chen: 0000-0003-1912-6490

Lane W. Martin: 0000-0003-1889-2513

Author Contributions

R.X. and L.W.M. conceived of the study and designed the experiment. R.X. carried out the film synthesis and electrical measurements. R.X., R.G., Y.D., X.L., A.R.D., and H.Z. performed the X-ray characterization. S.E.R.-L. performed the DFT calculation. S.S. conducted the RBS measurement. R.X. and H.L. performed the capacitor fabrication. R.X., R.G., Z.C., Y.Q., and S.-L.H. analyzed the data and discussed the results. J.B.N. and L.W.M. supervised the research. The manuscript was written through contributions of all authors. All authors have given approval to the final version of the manuscript.

Notes

The authors declare no competing financial interest.

ACKNOWLEDGMENTS

R.X. acknowledges support from the National Science Foundation under grant DMR-1708615. R.G. acknowledges support from the National Science Foundation under grant OISE-1545907. S.E.R.-L. acknowledges partial support from the Molecular Foundry (supported by the Office of Science, Office of Basic Energy Sciences, of the U.S. Department of Energy) and the Laboratory Directed Research and Development Program at the Lawrence Berkeley National Laboratory under contract number DE-AC02-05-CH11231. S.S. acknowledges support from the U.S. Department of Energy, Office of Science, Office of Basic Energy Sciences, under award number DE-SC-0012375 for development of ferroelectric thin films. H.L. acknowledges support from the National Science Foundation under grant DMR-1608938. Y.Q. acknowledges support from the National Science Foundation of China under grant 51472078. Z.C. and A.R.D. acknowledge partial support from the Army Research Office under grant W911NF-14-1-0104 and from Intel Corp. X.L. acknowledges the National Science Foundation of China under grant 11372002. S.L.H. acknowledges support from the National Science Foundation under the MRSEC program DMR-1420620. J.B.N. and L.W.M. acknowledge that this work was in-part funded by the U.S. Department of Energy, Office of Science, Office of Basic Energy Sciences, Materials Sciences and Engineering Division, under contract no. DE-AC02-05-CH11231: Materials Project Program KC23MP for the development of novel materials. This research used resources of the Advanced Photon Source, a U.S. Department of Energy (DOE) Office of Science User Facility operated for the DOE Office of Science by Argonne National Laboratory, under contract no. DE-AC02-06CH11357.

REFERENCES

(1) Setter, N.; Damjanovic, D.; Eng, L.; Fox, G.; Gevorgian, S.; Hong, S.; Kingon, A.; Kohlstedt, H.; Park, N. Y.; Stephenson, G. B.; Stolitchnov, I.; Taganstev, A. K.; Tylor, D. V.; Yamada, T.; Streiffer, S. Ferroelectric Thin Films: Review of Materials, Properties, and Applications. *J. Appl. Phys.* **2006**, *100*, 051606.

(2) Scott, J. F. Applications of Modern Ferroelectrics. *Science* **2007**, *315*, 954−959.

(3) Kimura, H.; Hanyu, T.; Kameyama, M.; Fujimori, Y.; Nakamura, T.; Takasu, H. Complementary Ferroelectric-Capacitor Logic for Low-Power Logic-in-Memory VLSI. *IEEE J. Solid-State Circuits* **2004**, *39*, 919−926.

(4) Whyte, J. R.; Gregg, J. M. A Diode for Ferroelectric Domain-Wall Motion. *Nat. Commun.* **2015**, *6*, 7361.

(5) Moazzami, R. Ferroelectric Thin Film Technology for Semiconductor Memory. *Semicond. Sci. Technol.* **1995**, *10*, 375−390.

(6) Hu, Z.; Tian, M.; Nysten, B.; Jonas, A. M. Regular Arrays of Highly Ordered Ferroelectric Polymer Nanostructures for Non-Volatile Low-Voltage Memories. *Nat. Mater.* **2009**, *8*, 62−67.

(7) Ramesh, R. Thin Film Ferroelectric Materials and Devices. In *Pb(Zr,Ti)O_3 Based Thin Film Ferroelectric Nonvolatile Memories*; Tuttle, B. A., Ed.; Springer Science and Business Media: New York, 1997; pp 145−165.

(8) Ihlefeld, J. F.; Harris, D. T.; Keech, R.; Jones, J. L.; Maria, J.-P.; Trolier-McKinstry, S. Scaling Effects in Perovskite Ferroelectrics: Fundamental Limits and Process-Structure-Property Relations. *J. Am. Ceram. Soc.* **2016**, *99*, 2537−2557.

(9) Nagarajan, V.; Junquera, J.; He, J. Q.; Jia, C. L.; Waser, R.; Lee, K.; Kim, Y. K.; Baik, S.; Zhao, T.; Ramesh, R.; Ghosez, Ph.; Rabe, K. M. Scaling of Structure and Electrical Properties in Ultrathin Epitaxial Ferroelectric Heterostructures. *J. Appl. Phys.* **2006**, *100*, 051609.

(10) Huang, C. W.; Chen, Z. H.; Chen, L. Thickness-Dependent Evolutions of Domain Configuration and Size in Ferroelectric and Ferroelectric-Ferroelastic Films. *J. Appl. Phys.* **2013**, *113*, 094101.

(11) Lee, H. N.; Nakhmanson, S. M.; Chisholm, M. F.; Christen, H. M.; Rabe, K. M.; Vanderbilt, D. Suppressed Dependence of Polarization on Epitaxial Strain in Highly Polar Ferroelectrics. *Phys. Rev. Lett.* **2007**, *98*, 217602.

(12) Fong, D. D.; Stephenson, G. B.; Streiffer, S. K.; Eastman, J. A.; Auciello, O.; Fuoss, P. H.; Thompson, C. Ferroelectricity in Ultrathin Perovskite Films. *Science* **2004**, *304*, 1650−1653.

(13) Pertsev, N. A.; Contreras, J. R.; Kukhar, V. G.; Hermanns, B.; Kohlstedt, H.; Waser, R. Coercive Field of Ultrathin Pb($Zr_{0.52}Ti_{0.48}$)O_3 Epitaxial Films. *Appl. Phys. Lett.* **2003**, *83*, 3356−3358.

(14) Kanzig, W. Mechanism of Fatigue in Ferroelectric Thin Films. *Phys. Stat. Sol. A* **1992**, *133*, 565−573.

(15) Tagantsev, A. K.; Landivar, M.; Colla, E.; Setter, N. Identification of Passive Layer in Ferroelectric Thin Films from Their Switching Parameters. *J. Appl. Phys.* **1995**, *78*, 2623−2630.

(16) Larsen, P. K.; Dormans, G. J. M.; Taylor, D. J.; Veldhoven; van, P. J. Ferroelectric Properties and Fatigue of $PbZr_{0.51}Ti_{0.49}O_3$ Thin Films of Varying Thickness: Blocking Layer Model. *J. Appl. Phys.* **1994**, *76*, 2405−2413.

(17) Martin, L. W.; Schlom, D. G. Advanced Synthesis Techniques and Routes to New Single-Phase Multiferroics. *Curr. Opin. Solid State Mater. Sci.* **2012**, *16*, 199−215.

(18) Martin, L. W.; Chu, Y. H.; Ramesh, R. Advances in The Growth and Characterization of Magnetic, Ferroelectric, and Multiferroic Oxide Thin Films. *Mater. Sci. Eng., R* **2010**, *68*, 89−133.

(19) Janovec, V. On The Theory of The Coercive Field of Single-Domain Crystals of $BaTiO_3$. *Czech. J. Phys.* **1958**, *8*, 3−15.

(20) Kay, H. F.; Dunn, J. W. Thickness Dependence of The Nucleation Field of Triglycine Sulphate. *Philos. Mag.* **1962**, *7*, 2027−2034.

DOI: 10.1021/acsnano.8b01399
ACS Nano 2018, 12, 4736−4743

(21) Chandra, P.; Dawber, M.; Littlewood, P. B.; Scott, J. F. Scaling of the Coercive Field with Thickness in Thin-Film Ferroelectrics. *Ferroelectrics* **2004**, *313*, 7−13.
(22) Bune, A. V.; Fridkin, V. M.; Ducharme, S.; Blinov, L. M.; Palto, S. P.; Sorokin, A. V.; Yudin, S. G.; Zlatkin, A. Two-Dimensional Ferroelectric Films. *Nature* **1998**, *391*, 874−877.
(23) Ducharme, S.; Fridkin, V. M.; Bune, A. V.; Palto, S. P.; Blinov, L. M.; Petukhova, N. N.; Yudin, S. G. Intrinsic Ferroelectric Coercive Field. *Phys. Rev. Lett.* **2000**, *84*, 175−178.
(24) Jo, J. Y.; Kim, Y. S.; Noh, T. W.; Yoon, J.-G.; Song, T. K. Coercive Fields in Ultrathin $BaTiO_3$ Capacitors. *Appl. Phys. Lett.* **2006**, *89*, 232909.
(25) Dawber, M.; Chandra, P.; Littlewood, P. B.; Scott, J. F. Depolarization Corrections to The Coercive Field in Thin-Film Ferroelectrics. *J. Phys.: Condens. Matter* **2003**, *15*, L393−L398.
(26) Xu, R.; Karthik, J.; Damodaran, A. R.; Martin, L. W. Stationary Domain Wall Contribution to Enhanced Ferroelectric Susceptibility. *Nat. Commun.* **2014**, *5*, 3120.
(27) Xu, R.; Liu, S.; Grinberg, I.; Karthik, J.; Damodaran, A. R.; Rappe, A. M.; Martin, L. W. Ferroelectric Polarization Reversal *via* Successive Ferroelastic Transitions. *Nat. Mater.* **2015**, *14*, 79−86.
(28) Liu, G.; Nan, C.-W. Thickness Dependence of Polarization in Ferroelectric Perovskite Thin Films. *J. Phys. D: Appl. Phys.* **2005**, *38*, 584−589.
(29) Liu, S.; Grinberg, I.; Rappe, A. M. Intrinsic Ferroelectric Switching from First Principles. *Nature* **2016**, *534*, 360−363.
(30) Perdew, J. P.; Zunger, A. Self-Interaction Correction to Density-Functional Approximations for Many-Electron Systems. *Phys. Rev. B: Condens. Matter Mater. Phys.* **1981**, *23*, 5048−5079.
(31) Kresse, G.; Furthmuller, J. Efficient Iterative Schemes for *ab initio* Total-Energy Calculations Using A Plane-Wave Basis Set. *Phys. Rev. B: Condens. Matter Mater. Phys.* **1996**, *54*, 11169−11186.
(32) Kresse, G.; Furthmuller, J. Efficiency of *ab initio* Total Energy Calculations for Metals and Semiconductors Using A Plane-Wave Basis Set. *Comput. Mater. Sci.* **1996**, *6*, 15−90.
(33) Pertsev, N. A.; Zembilgotov, A. G.; Tagantsev, A. K. Effect of Mechanical Boundary Conditions on Phase Diagrams of Epitaxial Ferroelectric Thin Films. *Phys. Rev. Lett.* **1998**, *80*, 1988−1991.
(34) Dieguez, O.; Rabe, K. M.; Vanderbilt, D. First-Principles Study of Epitaxial Strain in Perovskites. *Phys. Rev. B: Condens. Matter Mater. Phys.* **2005**, *72*, 144101.
(35) Tagantsev, A. K.; Pertsev, N. A.; Muralt, P.; Setter, N. Strain-Induced Diffuse Dielectric Anomaly and Critical Point in Perovskite Ferroelectric Thin Films. *Phys. Rev. B: Condens. Matter Mater. Phys.* **2001**, *65*, 012104.
(36) Oja, R.; Johnston, K.; Frantti, J.; Nieminen, R. M. Computational Study of (111) Epitaxially Strained Ferroelectric Perovskites $BaTiO_3$ and $PbTiO_3$. *Phys. Rev. B: Condens. Matter Mater. Phys.* **2008**, *78*, 094102.
(37) Monkhorst, H. J.; Pack, J. D. Special Points for Brillouin-Zone Integrations. *Phys. Rev. B* **1976**, *13*, 5188−5192.
(38) Kresse, G.; Joubert, D. From Ultrasoft Pseudopotentials to The Projector Augmented-Wave Method. *Phys. Rev. B: Condens. Matter Mater. Phys.* **1999**, *59*, 1758−1775.
(39) King-Smith, R. D.; Vanderbilt, D. Theory of Polarization of Crystalline Solids. *Phys. Rev. B: Condens. Matter Mater. Phys.* **1993**, *47*, 1651−1654.

DOI: 10.1021/acsnano.8b01399
ACS Nano 2018, 12, 4736−4743